Article

Hydrogenase Biomimetics with Redox-Active Ligands: Synthesis, Structure, and Electrocatalytic Studies on [Fe$_2$(CO)$_4$(κ^2-dppn)(μ-edt)] (edt = Ethanedithiolate; dppn = 1,8-bis(Diphenylphosphino)Naphthalene)

Shishir Ghosh [1,2,3,*] **, Shahed Rana** [2] **, Nathan Hollingsworth** [3] **, Michael G. Richmond** [4] **, Shariff E. Kabir** [2] **and Graeme Hogarth** [1,*]

[1]   Department of Chemistry, King's College London, Britannia House, 7 Trinity Street, London SE1 1DB, UK
[2]   Department of Chemistry, Jahangirnagar University, Savar, Dhaka 1342, Bangladesh;
      srana_ju@yahoo.com (S.R.); skabir_ju@yahoo.com (S.E.K.)
[3]   Department of Chemistry, University College London, 20 Gordon Street, London WC1H 0AJ, UK;
      Nathan.Hollingsworth@infineum.com
[4]   Department of Chemistry, University of North Texas, 1155 Union Circle, Box 305070, Denton, TX 76203, USA;
      cobalt@unt.edu
[*]   Correspondence: sghosh_006@yahoo.com (S.G.); graeme.hogarth@kcl.ac.uk (G.H.)

check for updates

Abstract: Addition of the bulky redox-active diphosphine 1,8-bis(diphenylphosphino)naphthalene (dppn) to [Fe$_2$(CO)$_6$(μ-edt)] (**1**) (edt = 1,2-ethanedithiolate) affords [Fe$_2$(CO)$_4$(κ^2-dppn)(μ-edt)] (**3**) as the major product, together with small amounts of a P–C bond cleavage product [Fe$_2$(CO)$_5$\{κ^1-PPh$_2$(1-C$_{10}$H$_7$)\}(μ-edt)] (**2**). The redox properties of **3** have been examined by cyclic voltammetry and it has been tested as a proton-reduction catalyst. It undergoes a reversible reduction at $E_{1/2}$ = −2.18 V and exhibits two overlapping reversible oxidations at $E_{1/2}$ = −0.08 V and $E_{1/2}$ = 0.04 V. DFT calculations show that while the Highest Occupied Molecular Orbital (HOMO) is metal-centred (Fe–Fe σ-bonding), the Lowest Unoccupied Molecular Orbital (LUMO) is primarily ligand-based, but also contains an antibonding Fe–Fe contribution, highlighting the redox-active nature of the diphosphine. It is readily protonated upon addition of strong acids and catalyzes the electrochemical reduction of protons at E_p = −2.00 V in the presence of CF$_3$CO$_2$H. The catalytic current indicates that it is one of the most efficient diiron electrocatalysts for the reduction of protons, albeit operating at quite a negative potential.

Keywords: hydrogenase biomimetics; dithiolate; proton-reduction; dppn; redox-active

1. Introduction

Interest in dithiolate-bridged diiron complexes [1–7] continues since they closely resemble the two-iron unit of the active site (H-cluster) of [FeFe]-hydrogenases [8,9]. Consequently, over the past 20 years, the synthesis, structural characterization, and redox properties of a diverse range of diiron-dithiolate complexes has been studied [1–7,10–13], most focusing on their role as electrocatalysts for proton-reduction [14,15], but also in hydrogen oxidation [16–22]. Diphosphine complexes, [Fe$_2$(CO)$_4$(κ^2-diphosphine)(μ-dithiolate)], containing a chelating diphosphine are of special interest as they contain an unsymmetrical, redox-active, diiron centre and normally protonate rapidly to afford the corresponding hydride-cations, [Fe$_2$(CO)$_4$(μ-H)(κ^2-diphosphine)(μ-dithiolate)]$^+$ [10–28]. Incorporation of redox-active ligands to the diiron center has also recently gained prominence [29–48] since the two redox systems can (potentially) interact electronically, acting in a cooperative manner [32,34,36],

thus mimicking the communication relay between diiron and tetrairon sites that regulates enzyme activity [8,9,36,46–48]. Diphosphines bearing an extended π-system in their backbone, such as 1,8-bis(diphenylphosphino)naphthalene (dppn) [49] and 2,3-bis(diphenylphosphino)maleic anhydride (bma) [50], are attractive surrogates of the tetrairon site due to the availability of a low-lying π*-orbital delocalised over the ligand backbone. Their incorporation may both lower the reduction potential of the biomimetic by accommodating the incoming electron in the π*-orbital, while also potentially facilitating electronic communication. Examples of diiron biomimetics containing these diphosphines are rare. In 2010, Schollhammer and co-workers reported studies on the bma complex, $[Fe_2(CO)_4(\mu\text{-pdt})(\kappa^2\text{-bma})]$, which has a relatively low reduction potential ($E_{1/2} = -0.89$ V); DFT studies showing that reduction is predominantly ligand-based [33]. Unfortunately, $[Fe_2(CO)_4(\mu\text{-pdt})(\kappa^2\text{-bma})]$ is inactive for proton-reduction, the lack of activity being attributed to the large gap between the redox potentials of the diiron and diphosphine sub-units, thus retarding proton-coupled electron-transfer [33]. In 2011, Camara and Rauchfuss reported the dppn complex, $[Fe_2(CO)_4\{\mu\text{-}(SCH_2)_2NCH_2Ph\}(\kappa^2\text{-dppn})]$, and showed that its radical cation could catalyze hydrogen oxidation in the presence of an oxidant, being a thousand times faster than the related trisubstituted derivative, $[Fe_2(CO)_3(PMe_3)\{\mu\text{-}(SCH_2)_2NCH_2Ph\}(\kappa^2\text{-dppv})]^+$ [dppv = cis-1,2-bis(diphenylphosphino)ethylene] [35]. As far as we are aware, $[Fe_2(CO)_4\{\mu\text{-}(SCH_2)_2NCH_2Ph\}(\kappa^2\text{-dppn})]$ was not examined for its proton-reduction behaviour; indeed, no diiron dppn complex has previously been examined in this capacity. Consequently, herein, we report the preparation and characterisation of the simple dppn complex, $[Fe_2(CO)_4(\kappa^2\text{-dppn})(\mu\text{-edt})]$ (**3**), together with an investigation of its proton-reduction ability.

2. Results and Discussion

2.1. Synthesis and Characterization

The Me_3NO-initiated reaction between $[Fe_2(CO)_6(\mu\text{-edt})]$ (**1**) and dppn in boiling MeCN gave two new diiron complexes: $[Fe_2(CO)_5\{\kappa^1\text{-PPh}_2(1\text{-}C_{10}H_7)\}(\mu\text{-edt})]$ (**2**) and $[Fe_2(CO)_4(\kappa^2\text{-dppn})(\mu\text{-edt})]$ (**3**) in an 8% and 44% yield, respectively (Scheme 1). While **3** was the anticipated product, isolation of **2** was unexpected since it results in a carbon–phosphorus bond cleavage of dppn, generally requiring more extreme robust experimental conditions than those employed here. Complex **2** could be formed via direct reaction between **1** and Ph_2PNaph (possibly present as an impurity), however, we have no evidence of this as the purity of the dppn used was confirmed spectroscopically by $^{31}P\{^1H\}$ NMR. Dppn activation at di- and polynuclear carbonyl centres has precedent; formation of diphenyl(1-naphthyl)phosphine $\{PPh_2(1\text{-}C_{10}H_7)\}$, being previously reported by us and others [51,52].
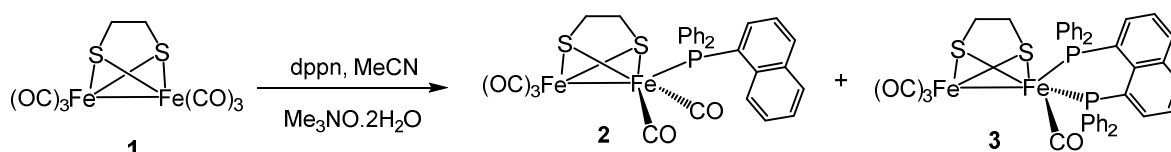
Scheme 1. Reaction of $[Fe_2(CO)_6(\mu\text{-edt})]$ (**1**) with dppn.

Structural characterization of both **2** and **3** was made on the basis of the crystal structure as shown in Figures 1 and 2, respectively. The former contains a diiron core coordinated by five carbonyls, a $PPh_2(1\text{-}C_{10}H_7)$, and a bridging edt ligand. The phosphine occupies an axial site, the Fe–P bond distance of 2.2442(6) Å being very similar to those reported for other $[Fe_2(CO)_5(\text{phosphine})(\mu\text{-edt})]$ complexes [26]. The Fe–Fe bond distance [2.5036(4) Å] is not affected by the phosphine substitution, being the same (within experimental error) as that in the parent hexacarbonyl **1** [2.5032(5) Å] [53]. Spectroscopic data indicate that the solid-state structure persists in solution. The carbonyl region of the IR spectrum shows a characteristic absorptions pattern for $[Fe_2(CO)_5(\text{phosphine})(\mu\text{-dithiolate})]$ complexes, while the $^{31}P\{^1H\}$ NMR spectrum displays a singlet at 61.1 ppm. The ^1H NMR spectrum is

not very informative, but shows two multiplets centred at 1.58 and 0.65 ppm (each integrating to two protons) attributed to the methylene protons of the edt-bridge, in addition to naphthyl and phenyl proton resonances in the aromatic region.
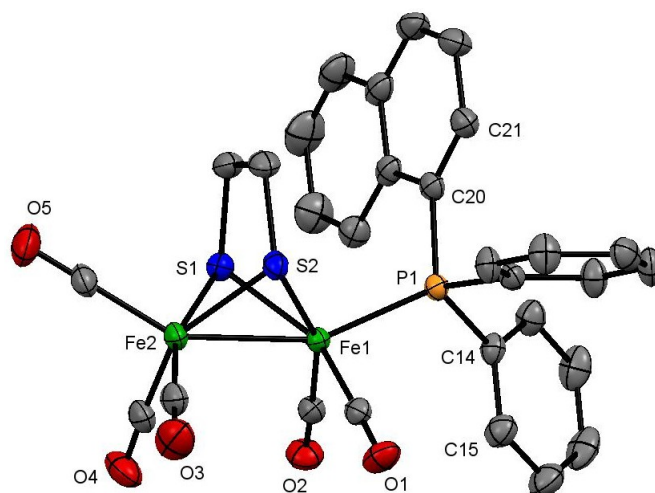

Figure 1. Molecular structure of $[Fe_2(CO)_5\{\kappa^1\text{-}PPh_2(1\text{-}C_{10}H_7)\}(\mu\text{-edt})]$ (**2**) showing 50% probability thermal ellipsoids. Hydrogen atoms are omitted for clarity. [Selected bond distances (Å) and angles (°): Fe(1)–Fe(2) 2.5036(4), Fe(1)–P(1) 2.2442(6), Fe(1)–S(1) 2.2501(6), Fe(1)–S(2) 2.2611(6), Fe(2)–S(1) 2.2520(6), Fe(2)–S(2) 2.2470(6); P(1)–Fe(1)–Fe(2) 155.755(18), P(1)–Fe(1)–S(1) 107.76(2), P(1)–Fe(1)–S(2) 106.08(2), P(1)–Fe(1)–C(1) 96.08(6), P(1)–Fe(1)–C(2) 95.55(6)].
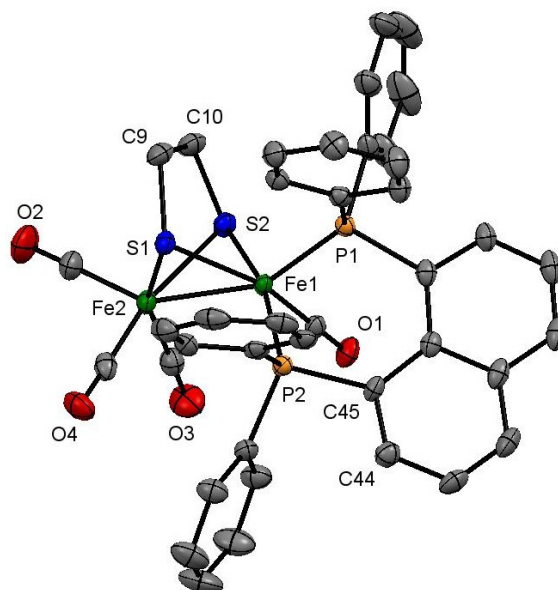

Figure 2. Molecular structure of one independent molecule of $[Fe_2(CO)_4(\kappa^2\text{-}dppn)(\mu\text{-edt})]$ (**3**) showing 50% probability thermal ellipsoids. Hydrogen atoms are omitted for clarity. [Selected bond distances (Å) and angles (°): Fe(1)–Fe(2) 2.5377(8), Fe(1)–P(1) 2.1756(9), Fe(1)–P(2) 2.1970(9), Fe(1)–S(1) 2.2478(9), Fe(1)–S(2) 2.2475(9), Fe(2)–S(1) 2.2526(9), Fe(2)–S(2) 2.2575(9); P(1)–Fe(1)–Fe(2) 155.21(3), P(2)–Fe(1)–Fe(2) 109.71(3), P(1)–Fe(1)–P(2) 88.14(3), P(1)–Fe(1)–S(1) 105.86(4), P(1)–Fe(1)–S(2) 107.90(3), P(1)–Fe(1)–C(1) 95.91(10)].

The molecular structure of **3** is complicated by the existence of two independent molecules in the asymmetric unit linked via π-interactions of the naphthalene backbones [C(39)–C(40) and C(76)–C(77) C···C 3.271–3.633 Å]. Both independent molecules are similar (bond lengths and angles do not differ significantly), consisting of a diiron framework coordinated by four carbonyls, a chelating dppn, and an

edt ligand, which bridges the diiron centre. The Fe(1)–Fe(2) bond distance [2.5377(8) Å] is slightly elongated as compared to that of the parent hexacarbonyl **1** [2.5032(5) Å] [53], probably to minimize the steric strain that accompanies dppn chelation. The dppn ligand is bound to Fe(1) occupying the apical and one of the basal coordination sites in the solid-state with a bite angle of 88.14(3)°. The Fe–P bond distances [Fe(1)–P(1) 2.1756(9) and Fe(1)–P(2) 2.1970(9) Å] are slightly shorter than that observed in **2**, but are within the range reported for related [$Fe_2(CO)_4(\kappa^2$-diphosphine)(μ-dithiolate)] complexes [16–27,33]. Solution spectroscopic data of **3** are consistent with the solid-state structure. The IR spectrum shows three absorptions at 2021 s, 1950 m, and 1901 w cm^{-1} for the carbonyls, while the $^{31}P\{^1H\}$ NMR spectrum displays only a singlet at 68.4 ppm. The latter is associated with the well-studied interconversion of apical-basal and dibasal isomers [19,20,22,41]. The ^1H NMR spectrum shows two doublets at 1.87 and 1.29 (*J* 7.8 Hz) ppm, each of which integrated for two protons, for the methylene protons of the edt-bridge in addition to naphthyl and phenyl proton resonances in the aromatic region. The $^{13}C\{^1H\}$ NMR spectrum at room temperature shows a broad resonance at 206.8 ppm attributed to the three carbonyls on the unsubstituted iron centre, and a sharp triplet at 220.3 ppm (J_{P-C} 19 Hz) for the fourth carbonyl. Upon cooling to −50 °C, the broad resonance splits into two sharp singlets at 215.7 and 206.6 ppm (ratio 2:1) consistent with freezing out of the trigonal rotation of the Fe(CO)$_3$ moiety. No change is seen to the other carbonyl resonance and the $^{31}P\{^1H\}$ NMR spectrum broadens only slightly at −50 °C showing that interconversion of axial and equatorial phosphorus sites remains rapid even at this temperature.

2.2. Protonation

Addition of a slight excess of HBF$_4$·Et$_2$O to a CH$_2$Cl$_2$ solution of **3** resulted in the immediate consumption of the latter as shown by IR spectroscopy. The appearance of new bands relating to two cationic hydrides was apparent as identified as dibasal [$Fe_2(CO)_4(\mu$-H)(κ^2-dppn)(μ-edt)][BF$_4$] (**3bb**) (2081 s, 2021 vs, 1950 m, 1898 w cm^{-1}) and apical-basal [$Fe_2(CO)_4(\mu$-H)(κ^2-dppn)(μ-edt)][BF$_4$] (**3ab**) (2097 vs, 2040 s, 1981 m, 1890 w cm^{-1}). Over time, absorptions associated with **3bb** diminished with concomitant growth of the υ(CO) bands for **3ab** being associated with the well-known isomerization of the kinetically formed hydride isomer to that which is thermodynamically more stable [16–22]. The rate of isomerization was dependent on acid concentration, being slower at low concentrations. With ca. 5 stoichiometric amounts of acid, immediate removal of excess acid and volatiles followed by washing in Et$_2$O allowed a clean IR spectrum of **3bb** to be obtained. Attempts to observe the cationic hydrides via NMR spectroscopy were unsuccessful, but it is clear from the IR data that they are formed rapidly and cleanly.

2.3. Electrochemistry

Complex **3** has been investigated by cyclic voltammetry (CV) in MeCN, which shows a reversible reduction wave at $E_{1/2}$ = −2.18 V (ΔE = 80 mV) and two overlapping reversible oxidative waves at $E_{1/2}$ = −0.08 V (ΔE = 80 mV) and $E_{1/2}$ = 0.04 V (ΔE = 60 mV) (Figure 3). The CV does not show any discernable change when the scan rate is varied (Figure S1). The reduction wave also shows good chemical reversibility (i_p^{ox}/i_p^{red} = ~0.85), and plots of reductive and oxidative peak currents of this reversible process against the square root of the scan rate give straight lines in support of a diffusion-controlled process on the CV time scale (Figure S2). The current function ($i_p/\sqrt{v}$) associated with reduction deviates from linearity only at slow scan rates (<0.05 V/s), indicating that more than one electron may be involved in reduction at longer time scales (Figure S3); otherwise, reduction of **3** is a one-electron process in MeCN. It is reduced at a similar potential to related [$Fe_2(CO)_4(\kappa^2$-diphosphine)(μ-dithiolate)] complexes containing non redox inactive diphosphines [21,22,25], which suggests that reduction is diiron-centered (as confirmed by DFT). Overlap of the two oxidative waves indicates that either the electrons are coming from separate parts of the same molecule, otherwise, a considerable gap would be seen between the two oxidation peaks, or **3** undergoes solvolysis after first oxidation to form probably [$Fe_2(CO)_3(MeCN)(\kappa^2$-dppn)($\mu$-edt)]$^+$,

which reduces at the second oxidation potential. We can rule out the solvolysis because it would render the first oxidation wave irreversible.
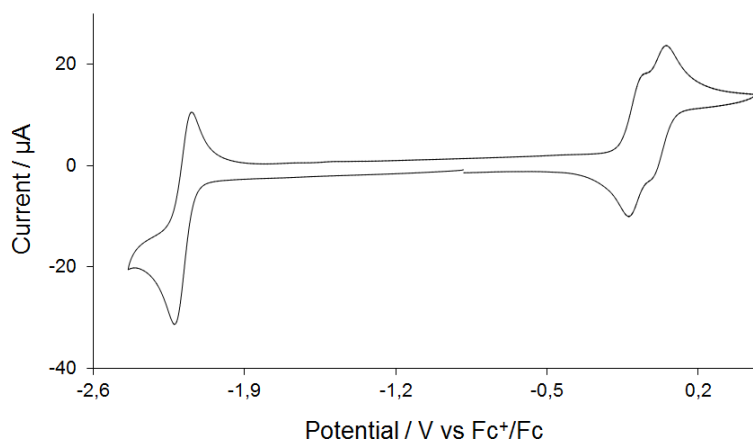

Figure 3. Cyclic Voltammogram (CV) of $[Fe_2(CO)_4(\kappa^2\text{-dppn})(\mu\text{-edt})]$ (**3**) in MeCN (1 mM solution, supporting electrolyte $[NBu_4][PF_6]$, scan rate $0.1\ V\cdot s^{-1}$, glassy carbon electrode, potential vs. Fc^+/Fc).

The nature of the HOMO and LUMO in **3** (Figure 4) was evaluated by DFT in order to better understand the role the dppn ligand plays, if any, in the observed reduction of proton to H_2 (*vide infra*). The structure of **3** was optimized, and the geometry-optimized structure (not shown) revealed excellent agreement with the experimentally determined structure depicted in Figure 2. The HOMO for **3** (left) is localized over the two iron centers and is best viewed as an in-phase Fe–Fe bond. The LUMO for **3** (right) exhibits the expected antibonding Fe–Fe interaction found in related derivatives along with a significant orbital contribution from the naphthalene π system, whose π^* nodal properties are evident. The composition of the LUMO is best described as ligand-based that contains an antibonding Fe–Fe contribution. The nodal pattern of the naphthalene π^* in the LUMO of **3** is comparable to the LUMO computed for the cluster $[Fe_4(CO)_{10}(\kappa^2\text{-dppn})(\mu_4\text{-O})]$ [54]. The dppn π^* system makes a much smaller contribution to the LUMO in the Fe_4 cluster relative to the antibonding metallic core. The enhanced catalytic behavior exhibited by **3**, vis-à-vis related derivatives of $[Fe_2(CO)_4(\kappa^2\text{-diphosphine})(\mu\text{-dithiolate})]$ whose ancillary diphosphine ligand does not contribute to the LUMO, signals the importance of the redox-active dppn ligand in promoting effective proton reduction.
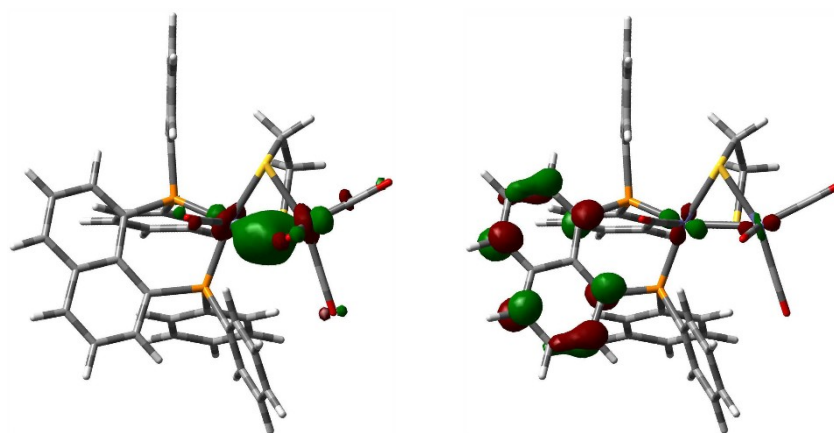

Figure 4. Plots of the HOMO (**left**) and LUMO (**right**) of $[Fe_2(CO)_4(\kappa^2\text{-dppn})(\mu\text{-edt})]$ (**3**) as computed by DFT. Both plots were printed at an isovalue of 0.06. For the M06-optimized structure of **3**, we have utilized the Stuttgart-Dresden effective core potential and SDD basis set for the iron atoms and a 6-31G(d′) basis set for the remaining non-metal atoms.

2.4. Catalysis

Complex **3** was tested as a proton reduction catalyst in the presence of CF_3CO_2H in MeCN solvent (Figure 5 and Figure S4). Selected CVs recorded upon sequential addition of 1–7 molar equivalents of acid are shown in Figure 5. Two new reduction peaks at $E_p = -2.00$ and -2.11 V are seen after addition of one molar equivalent of CF_3CO_2H. The reduction potential shows ca. 0.2 V positive shift after addition of CF_3CO_2H, suggesting the generation of cationic hydride. A small peak is also observed at the reduction potential of **3** at a very low acid concentration ($\leq$1 equivalent), which disappears at higher acid concentrations ($\geq$2 equivalents). Since CF_3CO_2H ($pK_a = 12.6$ in MeCN) is a much weaker acid than $HBF_4 \cdot Et_2O$ ($pK_a = -0.1$ in MeCN) [55], the latter is used for the protonation studies, which protonate **3** instantaneously, and we assume that protonation of **3** is slow at low CF_3CO_2H concentration. The height of the peaks at $E_p = -2.00$ and -2.11 V increase with acid concentration and is characteristic of electrocatalytic proton reduction by this complex at these potentials. It appears that **3** enters into the catalytic cycle via a chemical step (protonation), followed by an electrochemical reduction, which generates the neutral 35-electron complex $[Fe_2(CO)_4(\mu-H)(\kappa^2-dppn)(\mu-edt)]$. This neutral hydride can either protonate or undergo a further reduction before a second protonation to liberate hydrogen. The CVs also show curve-crossing i.e., build-up of reduction current on the return scan (ca. -1.80 V), in the presence of acid. This indicates that a more easily reducible product or intermediate is formed during catalysis, most probably via a slow chemical reaction [56–60]. This product or intermediate is sufficiently stable and its concentration increases as the concentration of acid is increased and it diffuses back to the electrode to undergo reduction at a more positive potential [56–60]. A plot of the catalytic current/noncatalytic current ratio (i_{cat}/i_p) against the concentration of acid is shown in Figure 6 for the first catalytic wave. The i_{cat}/i_p value increases to 20 after addition of 10 equivalents of CF_3CO_2H. To our knowledge, very few biomimetic diiron systems developed as models of the active site of [FeFe]-hydrogenases show such a high i_{cat}/i_p value [14,30,31,61]. For example, $[Fe_2(CO)_5(\kappa^1-IMes)(\mu-pdt)]$ [IMes = 1,3-bis(2,4,6-trimethylphenyl)imidazol-2-ylidene], which undergoes a two-electron reduction at -1.90 V vs. SCE, shows an i_{cat}/i_p value of ~4 after addition of 10 molar equivalents of CH_3CO_2H [61,62]. The i_{cat}/i_p value serves as a measure of the catalyst efficiency [61,63], and the values observed for **3** indicate that it is very efficient for the reduction of protons to H_2, although it operates at a very negative potential (-2.00 V). The highest i_{cat}/i_p value observed to date for electrocatalytic proton reduction is 38, shown by the nickel complex $[(P^{Ph}_2N^{Ph})Ni]^{2+}$ ($P^{Ph}_2N^{Ph}$ = 1,3,6-triphenyl-1-aza-3,6-diphosphacycloheptane) [64].
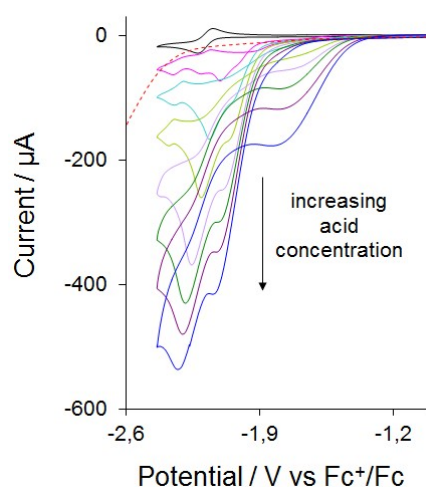

Figure 5. CVs of $[Fe_2(CO)_4(\kappa^2-dppn)(\mu-edt)]$ (**3**) in the absence of acid and in the presence of 1–7 equivalents of CF_3CO_2H (in MeCN, 1 mM solution, supporting electrolyte $[NBu_4][PF_6]$, scan rate 0.1 V·s^{-1}, glassy carbon electrode, potential vs. Fc$^+$/Fc). Response of 10 equivalents of CF_3CO_2H alone is shown with the red dotted line.

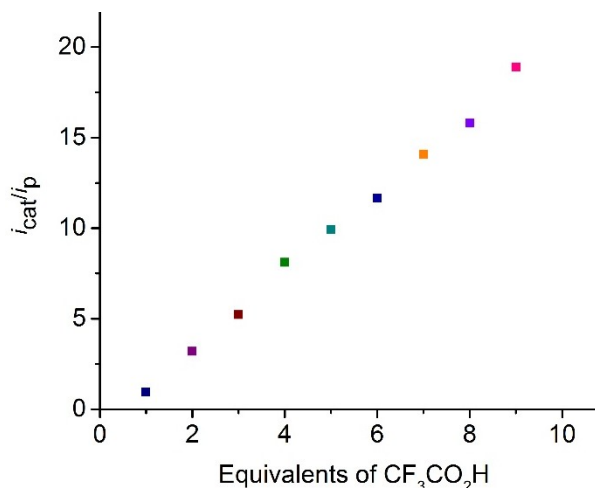**Figure 6.** Dependence of i_{cat}/i_p on CF_3CO_2H concentration for $[Fe_2(CO)_4(\kappa^2\text{-dppn})(\mu\text{-edt})]$ (**3**) at potentials of the first catalytic wave (in MeCN, 1 mM solution, 1–10 equivalents of CF_3CO_2H, supporting electrolyte $[NBu_4][PF_6]$, scan rate 0.1 V·s^{-1}, glassy carbon electrode).

3. Experimental

3.1. General Procedures

All reactions were carried out under a nitrogen atmosphere using standard Schlenk techniques. Reagent grade solvents were dried by the standard procedures and were freshly distilled prior to use. $[Fe_2(CO)_6(\mu\text{-edt})]$ (**1**) was synthesized according to the literature procedure [65]. IR spectra were recorded on a Shimadzu FTIR 8101 spectrophotometer (Shimadzu Corporation, Kyoto, Japan) while the NMR spectra were recorded on a Bruker DPX 400 instrument (Billerica, MA, USA). The chemical shifts were referenced to residual solvent resonances or external 85% H_3PO_4 in ^{1}H and ^{31}P spectra, respectively. Elemental analyses were performed in the Microanalytical Laboratories of Wazed Miah Science Research Centre at Jahangirnagar University (Dhaka, Bangladesh). Preparative thin layer chromatography was carried out on 1 mm plates prepared from silica gel GF254 (type 60, E. Merck) at Jahangirnagar University.

3.2. Synthesis

Me$_3$NO (21 mg, 0.279 mmol) was added to a MeCN solution (15 mL) of **1** (100 mg, 0.269 mmol) and dppn (134 mg, 0.270 mmol), and the mixture was heated to reflux for 1.5 h. After cooling to room temperature, volatiles were removed under reduced pressure and the residue chromatographed by Thin Layer Chromatography (TLC) on silica gel. Elution with hexane/CH_2Cl_2 (4:1, v/v) developed three bands. The faster-moving band was unreacted **1** (trace). The second and third bands yielded $[Fe_2(CO)_5\{\kappa^1\text{-PPh}_2(1\text{-C}_{10}H_7)\}(\mu\text{-edt})]$ (**2**) (14 mg, 8%) as red crystals and $[Fe_2(CO)_4(\kappa^2\text{-dppn})(\mu\text{-edt})]$ (**3**) (97 mg, 44%) as green crystals, respectively, after recrystallization from hexane/CH_2Cl_2 at 4 °C. Data for **2**: Anal. Calcd. for $C_{29}H_{21}Fe_2O_5PS_2$: C, 53.07; H, 3.23. Found: C, 53.81; H, 3.36%. IR (υ(CO), CH_2Cl_2): 2047 s, 1985 s, 1933 w cm^{-1}. ^{1}H NMR (CDCl$_3$): δ 8.11 (d, J 8.4, 1H), 7.89 (m, 2H), 7.72 (m, 4H), 7.53 (t, J 7.6, 1H), 7.44 (m, 6H), 7.21 (m, 2H), 6.94 (dd, J 12.5, 7.6, 1H), 1.58 (m, 2H), 0.65 (m, 2H). ^{31}P{^{1}H} NMR (CDCl$_3$): δ 61.1 (s). Data for **3**: Anal. Calcd. for $C_{40}H_{30}Fe_2O_4P_2S_2$: C, 59.13; H, 3.72. Found: C, 60.01; H, 3.86%. IR (υ(CO), CH_2Cl_2): 2021 s, 1950 m, 1901 w cm^{-1}. ^{1}H NMR (CD$_2$Cl$_2$, 273 K): δ 8.11 (d, J 7.1, 2H), 7.65 (d, J 7.1, 8H), 7.38 (d, J 7.1, 6H), 7.31 (s, 2H), 7.17 (s, 8H), 1.87 (d, J 7.8, 2H), 1.29 (d, J 7.8, 2H). ^{31}P{^{1}H} NMR (CD$_2$Cl$_2$): δ 68.4 (s). ^{13}C{^{1}H} NMR (CD$_2$Cl$_2$, 233 K): δ 220.2 (t, J 19, CO), 215.7 (s, 2CO), 206.6 (s, CO), 141.1 (t, J 21), 137.2 (t, J 14), 135.9 (s), 135.7 (d, J 9), 135.0 (s), 133.4 (d, 30), 132.7 (s), 131.8 (t, J 19), 130.5 (d, J 23), 129.4 (s), 128.0 (s), 127.6 (s), 124.8 (s), 35.1 (s, Me). (CD$_2$Cl$_2$, 298 K) 220.3 (t, J 19, CO), 206.8 (br, 3CO). Other resonances were not affected by temperature.

3.3. Protonation Experiments

To a CH_2Cl_2 solution (ca. 2 mL) of **3** (made by dissolving 4.5 mg, 0.005 mmol), 2 molar equivalents of $HBF_4·Et_2O$ were added. The resultant acid-containing solution was immediately transferred to an IR cell and monitored over time.

3.4. X-Ray Crystallography

Single crystals of **2** and **3** suitable for X-ray diffraction were grown by slow diffusion of hexane into a CH_2Cl_2 solution at 4 °C. All geometric and crystallographic data were collected at 150(2) K on a Bruker SMART APEX CCD diffractometer (Billerica, MA, USA) using Mo-Kα radiation (λ = 0.71073 Å) [66]. Data reduction and integration were carried out with *SAINT+* [67], and absorption corrections were applied using the program *SADABS* [68]. The structures were solved by direct methods and refined by full-matrix least squares on F^2 [69]. All non-hydrogen atoms were refined anisotropically. The hydrogen atoms were placed in the calculated positions and their thermal parameters were linked to those of the atoms to which they were attached (riding model). The *SHELXTL PLUS* V6.10 program package was used for structure solution and refinement [69]. Final difference maps did not show any residual electron density of stereochemical significance. The details of the data collection and structure refinement are given in Table A1.

3.5. Electrochemical Studies

Electrochemistry was carried out in deoxygenated MeCN with 0.1 M TBAPF$_6$ as the supporting electrolyte. The working electrode was a 3 mm diameter glassy carbon electrode that was polished with 0.3 μm alumina slurry prior to each scan. The counter electrode was a Pt wire and the quasi-reference electrode was a silver wire. All CVs were referenced to the Fc$^+$/Fc redox couple. An Autolab potentiostat (EcoChemie, Utrecht, Netherlands) was used for all electrochemical measurements. Catalysis studies were carried out by adding equivalents of CF_3CO_2H (Sigma-Aldrich, St. Louis, MO, USA).

3.6. Computational Methodology and Modeling Details

The DFT calculations were performed with the hybrid meta exchange-correlation functional M06 [70], as implemented by the Gaussian 09 program package [71]. The Fe [72] atoms were described by Stuttgart-Dresden effective core potentials (ecp) and an Stuttgart-Dresden (SDD) basis set, while a 6-31G(d') basis set was employed for all second row elements, and a 6-31G* basis set utilized for third row elements. The computed DFT structure for **3** represents a fully optimized ground state based on the positive eigenvalues displayed by the analytical Hessian.

4. Conclusions

The diiron-dithiolate $[Fe_2(CO)_4(\kappa^2\text{-dppn})(\mu\text{-edt})]$ (**3**) containing a chelating dppn ligand has been synthesized from the reaction between $[Fe_2(CO)_6(\mu\text{-edt})]$ (**1**) and dppn, together with a side product $[Fe_2(CO)_5\{\kappa^1\text{-PPh}_2(1\text{-C}_{10}H_7)\}(\mu\text{-edt})]$ (**2**) resulting from P–C bond cleavage. Both **2** and **3** have been characterized by single-crystal X-ray diffraction analysis and structural features are unexceptional. DFT calculations on **3** show that while the HOMO is based exclusively at the diiron centre, the LUMO has a significant contribution from the naphthalene π-system, showing that the dppn ligand is an integral part of the redox system. Cyclic voltammetry reveals that it undergoes a reversible part ligand based reduction and displays two overlapping reversible metal-centred oxidations in MeCN. Control experiments confirm that **3** is readily protonated to give the cationic hydrides tentatively identified as dibasal $[Fe_2(CO)_4(\mu\text{-H})(\kappa^2\text{-dppn})(\mu\text{-edt})][BF_4]$ (**3bb**) and apical-basal $[Fe_2(CO)_4(\mu\text{-H})(\kappa^2\text{-dppn})(\mu\text{-edt})][BF_4]$ (**3ab**); the former hydride is less stable and transforms into the latter hydride over time. Complex **3** has been examined as an electrocatalyst for proton-reduction. Analysis of electrocatalytic data indicates that it operates at a very negative potential (ca. −2 V), showing that even after protonation, reduction is primarily ligand based. However, that it is an active

catalyst shows that there must be electronic communication between the dppn and diiron centres. Indeed, **3** is one of the most efficient diiron biomimetics reported to date and thus intramolecular electron-transfer within the cationic dihydride must be efficient. Thus, the redox-active dppn ligand plays a critical role in the observed electrochemical proton-reduction. The exact nature of this remains unknown and in future work we will aim to better understand and exploit this electron coupling.

Supplementary Materials: The following are available online at http://www.mdpi.com/2304-6740/6/4/122/s1, Figure S1: CVs of [Fe$_2$(CO)$_4$(κ^2-dppn)(μ-edt)] (3) at various scan rates as shown in the legend (in MeCN, 1 mM solution, supporting electrolyte [NBu$_4$][PF$_6$], scan rate 0.1 V·s^{-1}, glassy carbon electrode, potential vs Fc$^+$/Fc), Figure S2: Scan rate dependence of the cathodic and anodic peak currents for the reduction of [Fe$_2$(CO)$_4$(κ^2-dppn)(μ-edt)] (3) in MeCN (1 mM solution, supporting electrolyte [NBu$_4$][PF$_6$], glassy carbon electrode, potential vs Fc$^+$/Fc). Lines show best linear fit of data, Figure S3: Scan rate (ν) dependence of the current function ($i_p/\sqrt{\nu}$) for the reduction of [Fe$_2$(CO)$_4$(κ^2-dppn)(μ-edt)] (3) (1 mM solution in MeCN, supporting electrolyte [NBu$_4$][PF$_6$], glassy carbon electrode, potential vs Fc$^+$/Fc), Figure S4: CVs of [Fe$_2$(CO)$_4$(κ^2-dppn)(μ-edt)] (3) in the absence of acid and in the presence of 1–10 equivalents of CF$_3$CO$_2$H (in MeCN, 1 mM solution, supporting electrolyte [NBu$_4$][PF$_6$], scan rate 0.1 V·s^{-1}, glassy carbon electrode, potential vs Fc$^+$/Fc).

Author Contributions: Synthetic works were carried out by S.G. and S.R. with input from S.E.K. and G.H. Protonation, electrochemistry and catalytic studies were carried out by S.G. and N.H. with input from G.H. DFT calculations were carried out by M.G.R. with input from G.H. and S.G. The manuscript was written jointly by S.G. and G.H.

Funding: This research was funded by Commonwealth Scholarship to S.G. and King's College London.

Acknowledgments: M.G.R. acknowledges the Robert A. Welch Foundation (grant B-1093) for continued research support. The DFT calculations reported here were performed at UNT through CASCaM, which is an NSF-supported facility (CHE-1531468).

Conflicts of Interest: The authors declare no conflict of interest.

Appendix

CCDC 1861465 (for **2**) and CCDC 1861466 (for **3**) contain the supplementary crystallographic data for this paper. These data can be obtained free of charge from The Cambridge Crystallographic Data Centre via www.ccdc.cam.ac.uk/data_request/cif.

Table A1. Crystal data and structure refinement details.

Complex	2	3
Empirical formula	C$_{29}$H$_{21}$Fe$_2$O$_5$PS$_2$	C$_{41}$H$_{32}$Fe$_2$O$_4$P$_2$S$_2$
Formula weight	656.25	897.33
Temperature (K)	150(2)	150(2)
Wavelength (Å)	0.71073	0.71073
Crystal system	orthorhombic	triclinic
Space group	*Pbca*	*P*-1
Unit cell dimensions		
a (Å)	17.2973(10)	14.310(3)
b (Å)	15.6070(9)	16.653(4)
c (Å)	20.9270(12)	18.478(4)
α (°)	90	115.075(3)
β (°)	90	94.809(4)
γ (°)	90	99.124(3)
Volume (Å^3)	5649.4(6)	3881.2(14)
Z	8	4
Density (calculated) (Mg/m^3)	1.543	1.536
Absorption coefficient (mm^{-1})	1.269	1.117
F(000)	2672	1832
Crystal size (mm^3)	0.26 × 0.13 × 0.13	0.28 × 0.26 × 0.08
θ range for data collection (°)	2.79 to 28.30	2.48 to 28.34

Table A1. *Cont.*

Complex	2	3
Index ranges	$-22 \leq h \leq 22$, $-20 \leq k \leq 20$, $-27 \leq l \leq 26$	$-18 \leq h \leq 18$, $-21 \leq k \leq 21$, $-23 \leq l \leq 23$
Reflections collected	46753	32780
Independent reflections [R_{int}]	6896 [R_{int} = 0.0427]	17593 [R_{int} = 0.0379]
Max. and min. transmission	0.8524 and 0.7338	0.9159 and 0.7450
Data/restraints/parameters	6896/0/352	17593/0/955
Goodness of fit on F^2	1.056	1.022
Final R indices [$I > 2\sigma(I)$]	R_1 = 0.0378, wR_2 = 0.0837	R_1 = 0.0512, wR_2 = 0.1339
R indices (all data)	R_1 = 0.0501, wR_2 = 0.0879	R_1 = 0.0740, wR_2 = 0.1484
Largest diff. peak and hole (e·Å^{-3})	0.479 and -0.276	1.378 and -0.821

References

1. Tard, C.; Pickett, C.J. Structural and Functional Analogues of the Active Sites of the [Fe]-, [NiFe]-, and [FeFe]-Hydrogenases. *Chem. Rev.* **2009**, *109*, 2245–2274. [CrossRef] [PubMed]

2. Sun, L.; Åkermark, B.; Ott, S. Iron hydrogenase active site mimics in supramolecular systems aiming for light-driven hydrogen production. *Coord. Chem. Rev.* **2005**, *249*, 1653–1663. [CrossRef]

3. Evans, D.J.; Pickett, C.J. Chemistry and the hydrogenases. *Chem. Soc. Rev.* **2003**, *32*, 268–275. [CrossRef] [PubMed]

4. Georgakaki, I.P.; Thomson, L.M.; Lyon, E.J.; Hall, M.B.; Darensbourg, M.Y. Fundamental properties of small molecule models of Fe-only hydrogenase: Computations relative to the definition of an entatic state in the active site. *Coord. Chem. Rev.* **2003**, *238–239*, 255–266. [CrossRef]

5. Rauchfuss, T.B. Research on Soluble Metal Sulfides: From Polysulfido Complexes to Functional Models for the Hydrogenases. *Inorg. Chem.* **2004**, *43*, 14–26. [CrossRef] [PubMed]

6. Liu, X.; Ibrahim, S.K.; Tard, C.; Pickett, C.J. Iron-only hydrogenase: Synthetic, structural and reactivity studies of model compounds. *Coord. Chem. Rev.* **2005**, *249*, 1641–1652. [CrossRef]

7. Lubitz, W.; Ogata, H.; Rudiger, O.; Reijerse, E. Hydrogenases. *Chem. Rev.* **2014**, *114*, 4081–4148. [CrossRef] [PubMed]

8. Peters, J.W.; Lanzilotta, W.N.; Lemon, B.; Seefeldt, L.C. X-ray Crystal Structure of the Fe-only Hydrogenase (CpI) from *Clostridium pasteurianum* to 1.8 Angstrom Resolution. *Science* **1998**, *282*, 1853–1858. [CrossRef] [PubMed]

9. Nicolet, Y.; Piras, C.; Legrand, P.; Hatchikian, C.E.; Fontecilla-Camps, J.C. *Desulfovibrio desulfuricans* iron hydrogenase: The structure shows unusual coordination to an active site Fe binuclear center. *Structure* **1999**, *7*, 13–23. [CrossRef]

10. Li, Y.; Rauchfuss, T.B. Synthesis of Diiron(I) Dithiolato Carbonyl Complexes. *Chem. Rev.* **2016**, *116*, 7043–7077. [CrossRef] [PubMed]

11. Apfel, U.-P.; Pétillon, F.Y.; Schollhammer, P.; Talarmin, J.; Weigand, W. [FeFe] Hydrogenase Models: An Overview. In *Bioinspired Catalysis*; Schollhammer, P., Weigand, W., Eds.; Wiley-VCH: Weinheim, Germany, 2014.

12. Lansing, J.C.; Manor, B.C.; Rauchfuss, T.B. Hydrogenase Models. In *Encyclopedia of Inorganic and Bioinorganic Chemistry*; John Wiley & Sons, Inc.: Hoboken, NJ, USA, 2014; pp. 1–21.

13. Tschierlei, S.; Ott, S.; Lomoth, R. Spectroscopically Characterized Intermediates of Catalytic H_2 Formation by [FeFe] Hydrogenase Models. *Energy Environ. Sci.* **2011**, *4*, 2340–2352. [CrossRef]

14. Felton, G.A.N.; Mebi, C.A.; Petro, B.J.; Vannucci, A.K.; Evans, D.H.; Glass, R.S.; Lichtenberger, D.L. Review of Electrochemical Studies of Complexes Containing the Fe_2S_2 Core Characteristic of [FeFe]-Hydrogenases Including Catalysis by These Complexes of the Reduction of Acids to Form Dihydrogen. *J. Organomet. Chem.* **2009**, *694*, 2681–2699. [CrossRef]

15. Gloaguen, F. Electrochemistry of Simple Organometallic Models of Iron–Iron Hydrogenases in Organic Solvent and Water. *Inorg. Chem.* **2016**, *55*, 390–398. [CrossRef] [PubMed]

16. Ezzaher, S.; Capon, J.-F.; Gloaguen, F.; Pétillon, F.Y.; Schollhammer, P.; Talarmin, J.; Kervarec, N. Influence of a Pendant Amine in the Second Coordination Sphere on Proton Transfer at a Dissymmetrically Disubstituted Diiron System Related to the $[2Fe]_H$ Subsite of $[FeFe]H_2$ase. *Inorg. Chem.* **2009**, *48*, 2–4. [CrossRef] [PubMed]

17. Wang, N.; Wang, M.; Liu, J.; Jin, K.; Chen, L.; Sun, L. Preparation, Facile Deprotonation, and Rapid H/D Exchange of the μ-Hydride Diiron Model Complexes of the [FeFe]-Hydrogenase Containing a Pendant Amine in a Chelating Diphosphine Ligand. *Inorg. Chem.* **2009**, *48*, 11551–11558. [CrossRef] [PubMed]

18. Ezzaher, S.; Capon, J.-F.; Dumontet, N.; Gloaguen, F.; Pétillon, F.Y.; Schollhammer, P.; Talarmin, J. Electrochemical study of the role of a H-bridged, unsymmetrically disubstituted diiron complex in proton reduction catalysis. *J. Electroanal. Chem.* **2009**, *626*, 161–170. [CrossRef]

19. Ezzaher, S.; Capon, J.-F.; Gloaguen, F.; Pétillon, F.Y.; Schollhammer, P.; Talarmin, J. Evidence for the Formation of Terminal Hydrides by Protonation of an Asymmetric Iron Hydrogenase Active Site Mimic. *Inorg. Chem.* **2007**, *46*, 3426–3428. [CrossRef] [PubMed]

20. Adam, F.I.; Hogarth, G.; Kabir, S.E.; Richards, I. Models of the iron-only hydrogenase: Synthesis and protonation of bridge and chelate complexes $[Fe_2(CO)_4\{Ph_2P(CH_2)_nPPh_2\}(\mu-pdt)]$ (n = 2–4)—Evidence for a terminal hydride intermediate. *C. R. Chim.* **2008**, *11*, 890–905. [CrossRef]

21. Ghosh, S.; Sanchez, B.E.; Richards, I.; Haque, M.N.; Holt, K.B.; Richmond, M.G.; Hogarth, G. Biomimetics of the [FeFe]-hydrogenase enzyme: Identification of kinetically favoured apical-basal $[Fe_2(CO)_4(\mu-H)\{\kappa^2-Ph_2PC(Me_2)PPh_2\}(\mu-pdt)]^+$ as a proton-reduction catalyst. *J. Organomet. Chem.* **2016**, *812*, 247–258. [CrossRef]

22. Ghosh, S.; Hogarth, G.; Hollingsworth, N.; Holt, K.B.; Richards, I.; Richmond, M.G.; Sanchez, B.E.; Unwin, D. Models of the iron-only hydrogenase: A comparison of chelate and bridge isomers of $Fe_2(CO)_4\{Ph_2PN(R)PPh_2\}(\mu-pdt)$ as proton-reduction catalysts. *Dalton Trans.* **2013**, *42*, 6775–6792. [CrossRef] [PubMed]

23. Adam, F.I.; Hogarth, G.; Richards, I.; Sanchez, B.E. Models of the iron-only hydrogenase: Structural studies of chelating diphosphine complexes $[Fe_2(CO)_4(\mu-pdt)(\kappa^2-P,P'-diphosphine)]$. *Dalton Trans.* **2007**, 2495–2498. [CrossRef] [PubMed]

24. Adam, F.I.; Hogarth, G.; Richards, I. Models of the iron-only hydrogenase: Reactions of $[Fe_2(CO)_6(\mu-pdt)]$ with small bite-angle diphosphines yielding bridge and chelate diphosphine complexes $[Fe_2(CO)_4(diphosphine)(\mu-pdt)]$. *J. Organomet. Chem.* **2007**, *692*, 3957–3968. [CrossRef]

25. Ezzaher, S.; Capon, J.-F.; Gloaguen, F.; Pétillon, F.Y.; Schollhammer, P.; Talarmin, J. Electron-Transfer-Catalyzed Rearrangement of Unsymmetrically Substituted Diiron Dithiolate Complexes Related to the Active Site of the [FeFe]-Hydrogenases. *Inorg. Chem.* **2007**, *46*, 9863–9872. [CrossRef] [PubMed]

26. Rana, S.; Ghosh, S.; Hossain, M.K.; Rahaman, A.; Hogarth, G.; Kabir, S.E. Hydrogenase biomimetics: Structural and spectroscopic studies on diphosphine-substituted derivatives of $Fe_2(CO)_6(\mu-edt)$ (edt = ethanedithiolate) and $Fe_2(CO)_6(\mu-tdt)$ (tdt = 1,3-toluenedithiolate). *Trans. Met. Chem.* **2016**, *41*, 933–942. [CrossRef]

27. Justice, A.K.; Zampella, G.; Gioia, L.D.; Rauchfuss, T.B.; van der Vlugt, J.I.; Wilson, S.R. Chelate Control of Diiron(I) Dithiolates Relevant to the [Fe−Fe]-Hydrogenase Active Site. *Inorg. Chem.* **2007**, *46*, 1655–1664. [CrossRef] [PubMed]

28. Ridley, F.; Ghosh, S.; Hogarth, G.; Hollingsworth, N.; Holt, K.B.; Unwin, D.G. Fluorinated models of the iron-only hydrogenase: An electrochemical study of the influence of an electron-withdrawing bridge on the proton reduction overpotential and catalyst stability. *J. Electroanal. Chem.* **2013**, *703*, 14–22. [CrossRef]

29. Rauchfuss, T.B. Diiron Azadithiolates as Models for the [FeFe]-Hydrogenase Active Site and Paradigm for the Role of the Second Coordination Sphere. *Acc. Chem. Res.* **2015**, *48*, 2107–2116. [CrossRef] [PubMed]

30. Ghosh, S.; Rahaman, A.; Holt, K.B.; Nordlander, E.; Richmond, M.G.; Kabir, S.E.; Hogarth, G. Hydrogenase biomimetics with redox-active ligands: Electrocatalytic proton reduction by $[Fe_2(CO)_4(\kappa^2-diamine)(\mu-edt)]$ (diamine = 2,2′-bipy,1,10-phen). *Polyhedron* **2016**, *116*, 127–135. [CrossRef]

31. Ghosh, S.; Hogarth, G.; Hollingsworth, N.; Holt, K.B.; Kabir, S.E.; Sanchez, B.E. Hydrogenase biomimetics: Fe$_2$(CO)$_4$(μ-dppf)(μ-pdt)(dppf = 1,1'-bis(diphenylphosphino) ferrocene) both a proton-reduction and hydrogen oxidation catalyst. *Chem. Commun.* **2014**, *50*, 945–947. [CrossRef] [PubMed]

32. Greco, C. H$_2$ Binding and Splitting on a New-Generation [FeFe]-Hydrogenase Model Featuring a Redox-Active Decamethylferrocenyl Phosphine Ligand: A Theoretical Investigation. *Inorg. Chem.* **2013**, *52*, 1901–1908. [CrossRef] [PubMed]

33. Youtao, S.; Charreteur, K.; Capon, J.-F.; Gloaguen, F.; Pétillon, F.Y.; Schollhammer, P.; Talarmin, J. Non-innocent bma ligand in a dissymetrically disubstituted diiron dithiolate related to the active site of the [FeFe] hydrogenases. *J. Inorg. Biochem.* **2010**, *104*, 1038–1042.

34. Camara, J.M.; Rauchfuss, T.B. Combining Acid-base, Redox and Substrate Binding Functionalities to Give a Complete Model for the [FeFe]-hydrogenase. *Nat. Chem.* **2012**, *4*, 26–30. [CrossRef] [PubMed]

35. Camara, J.M.; Rauchfuss, T.B. Mild Redox Complementation Enables H$_2$ Activation by [FeFe]-Hydrogenase Models. *J. Am. Chem. Soc.* **2011**, *133*, 8098–8101. [CrossRef] [PubMed]

36. Tard, C.; Liu, X.M.; Ibrahim, S.K.; Bruschi, M.; Gioia, L.D.; Davies, S.C.; Yang, X.; Wang, L.S.; Sawers, G.; Pickett, C.J. Synthesis of the H-cluster Framework of Iron-only Hydrogenase. *Nature* **2005**, *433*, 610–613. [CrossRef] [PubMed]

37. Gimbert-Suriñach, C.; Bhadbhade, M.; Colbran, S.B. Bridgehead Hydrogen Atoms Are Important: Unusual Electrochemistry and Proton Reduction at Iron Dimers with Ferrocenyl-Substituted Phosphido Bridges. *Organometallics* **2012**, *31*, 3480–3491. [CrossRef]

38. Greco, C.; Gioia, L.D. A Theoretical Study on the Enhancement of Functionally Relevant Electron Transfers in Biomimetic Models of [FeFe]-Hydrogenases. *Inorg. Chem.* **2011**, *50*, 6987–6995. [CrossRef] [PubMed]

39. Orain, P.-Y.; Capon, J.-F.; Gloaguen, F.; Pétillon, F.Y.; Schollhammer, P.; Talarmin, J.; Zampella, G.; Gioia, L.D.; Roisnel, T. Investigation on the Protonation of a Trisubstituted [Fe$_2$(CO)$_3$(PPh$_3$)(κ^2-phen)(μ-pdt)] Complex: Rotated versus Unrotated Intermediate Pathways. *Inorg. Chem.* **2010**, *49*, 5003–5008. [CrossRef] [PubMed]

40. Ezzaher, S.; Orain, P.-Y.; Capon, J.-F.; Gloaguen, F.; Pétillon, F.; Roisnel, T.; Schollhammer, P.; Talarmin, J. First Insights into the Protonation of Dissymetrically Disubstituted Di-iron Azadithiolate Models of the [FeFe]H$_2$ases Active Site. *Chem. Commun.* **2008**, 2547–2549. [CrossRef] [PubMed]

41. Capon, J.-F.; Gloaguen, F.; Pétillon, F.Y.; Schollhammer, P.; Talarmin, J. Organometallics Diiron Complex Chemistry Related to the [2Fe]$_H$ Subsite of [FeFe]H$_2$ase. *Eur. J. Inorg. Chem.* **2008**, 4671–4681. [CrossRef]

42. Orain, P.-Y.; Capon, J.-F.; Kervarec, N.; Gloaguen, F.; Pétillon, F.; Pichon, R.; Schollhammer, P.; Talarmin, J. Use of 1,10-Phenanthroline in Diiron Dithiolate Derivatives Related to the [Fe–Fe] Hydrogenase Active Site. *Dalton Trans.* **2007**, 3754–3756. [CrossRef] [PubMed]

43. Roy, S.; Groy, T.L.; Jones, A.K. Biomimetic Model for [FeFe]-hydrogenase: Asymmetrically Disubstituted Diiron Complex with a Redox-active 2,2'-Bipyridyl Ligand. *Dalton Trans.* **2013**, *42*, 3843–3853. [CrossRef] [PubMed]

44. Liu, Y.-C.; Yen, T.-H.; Chu, K.-T.; Chiang, M.-H. Utilization of Non-Innocent Redox Ligands in [FeFe] Hydrogenase Modeling for Hydrogen Production. *Comments Inorg. Chem.* **2016**, *36*, 141–181. [CrossRef]

45. Liu, Y.-C.; Lee, C.-H.; Lee, G.-H.; Chiang, M.-H. Influence of a Redox-Active Phosphane Ligand on the Oxidations of a Diiron Core Related to the Active Site of Fe-only Hydrogenase. *Eur. J. Inorg. Chem.* **2011**, 1155–1162. [CrossRef]

46. Hsieh, C.-H.; Ding, S.; Erdem, Ö.F.; Crouthers, D.J.; Liu, T.; McCrory, C.C.L.; Lubitz, W.; Popescu, C.V.; Reibenspies, J.H.; Hall, M.B.; et al. Redox active iron nitrosyl units in proton reduction electrocatalysis. *Nat. Commun.* **2014**, *5*, 3684. [CrossRef] [PubMed]

47. Yen, T.-H.; He, Z.-C.; Lee, G.-H.; Tseng, M.-C.; Shen, Y.-H.; Tseng, T.-W.; Liaw, W.-F.; Chiang, M.-H. Reduced thione ligation is preferred over neutral phosphine ligation in diiron biomimics regarding electronic functionality: A spectroscopic and computational investigation. *Chem. Commun.* **2017**, *53*, 332–335. [CrossRef] [PubMed]

48. Liu, Y.-C.; Yen, T.-H.; Tseng, Y.-J.; Hu, C.-H.; Lee, G.-H.; Chiang, M.-H. Electron Delocalization from the Fullerene Attachment to the Diiron Core within the Active-Site Mimics of [FeFe]Hydrogenase. *Inorg. Chem.* **2012**, *51*, 5997–5999. [CrossRef] [PubMed]

49. Costa, T.; Schmidbaur, H. 1,8-Naphthalenediylbis(dimethylphosphane): Steric Influence on Methylation and Borylation. *Chem. Ber.* **1982**, *115*, 1374–1378. [CrossRef]

50. Fenske, D.; Becher, H.J. Synthesis and Properties of Derivatives of 2,3-Bis(diphenylphosphino)maleic Anhydride as a Contribution to the Problem of Colour, Conjugation, and Complex Formation of this Class of Compounds. *Chem. Ber.* **1975**, *108*, 2115–2123. [CrossRef]

51. Bruce, M.I.; Humphrey, P.A.; Okucu, S.; Schmutzler, R.; Skelton, B.W.; White, A.H. Reactions of 1,8-Bis(diphenylphosphino)naphthalene with $Os_3(CO)_{12}$: C–H and C–P Bond Cleavage Reactions. *J. Organomet. Chem.* **2004**, *689*, 2415–2420. [CrossRef]

52. Kabir, S.E.; Ahmed, F.; Ghosh, S.; Hassan, M.R.; Islam, M.S.; Sharmin, A.; Tocher, D.A.; Haworth, D.T.; Lindeman, S.V.; Siddiquee, T.A.; et al. Reactions of Rhenium and Manganese Carbonyl Complexes with 1,8-Bis(diphenylphosphino) naphthalene: Ligand Chelation, C–H and C–P Bond-cleavage Reactions. *J. Organomet. Chem.* **2008**, *693*, 2657–2665. [CrossRef]

53. Kabir, S.E.; Rahman, A.F.M.M.; Parvin, J.; Malik, K.M.A. Reexamination of the Reactivity of Iron Carbonyls with 1,2-Ethanedithiol. *Indian J. Chem.* **2003**, *42A*, 2518–2522.

54. Ghosh, S.; Holt, K.B.; Kabir, S.E.; Richmond, M.G.; Hogarth, G. Electrocatalytic proton reduction catalyzed by the low-valent tetrairon-oxo cluster $[Fe_4(CO)_{10}(\kappa^2\text{-dppn})(\mu_4\text{-O})]^{2-}$ [dppn = 1,1'-bis(diphenylphosphino)naphthalene]. *Dalton Trans.* **2015**, *44*, 5160–5169. [CrossRef] [PubMed]

55. Izutsu, K. *Acid-Base Dissociation Constants in Dipolar Aprotic Solvents*; IUPAC Chemical Data Series No. 35; Blackwell Scientific Publications: Oxford, UK, 1990.

56. Mejia-Rodriguez, R.; Chong, D.; Reibenspies, J.H.; Soriaga, M.P.; Darensbourg, M.Y. The Hydrophilic Phosphatriazaadamantane Ligand in the Development of H_2 Production Electrocatalysts: Iron Hydrogenase Model Complexes. *J. Am. Chem. Soc.* **2004**, *126*, 12004–12014. [CrossRef] [PubMed]

57. Ghosh, S.; Basak-Modi, S.; Richmond, M.G.; Nordlander, E.; Hogarth, G. Electrocatalytic proton reduction by thiolate-capped triiron clusters $[Fe_3(CO)_9(\mu_3\text{-SR})(\mu\text{-H})]$ (R = ^{i}Pr, ^{t}Bu). *Inorg. Chim. Acta* **2018**, *480*, 47–53. [CrossRef]

58. Chong, D.; Georgakaki, I.P.; Mejia-Rodriguez, R.; Sanabria-Chinchilla, J.; Soriaga, M.P.; Darensbourg, M.Y. Electrocatalysis of hydrogen production by active site analogues of the iron hydrogenase enzyme: Structure/function relationships. *Dalton Trans.* **2003**, 4158–4163. [CrossRef]

59. Felton, G.A.N.; Vannucci, A.K.; Chen, J.; Lockett, L.T.; Okumura, N.; Petro, B.J.; Zakai, U.I.; Evans, D.H.; Glass, R.S.; Lichtenberger, D.L. Hydrogen Generation from Weak Acids: Electrochemical and Computational Studies of a Diiron Hydrogenase Mimic. *J. Am. Chem. Soc.* **2007**, *129*, 12521–12530. [CrossRef] [PubMed]

60. Liu, Y.-C.; Chu, K.-T.; Jhang, R.-L.; Lee, G.-H.; Chiang, M.-H. [FeFe] hydrogenase active site modeling: A key intermediate bearing a thiolate proton and Fe hydride. *Chem. Commun.* **2013**, *49*, 4743–4745. [CrossRef] [PubMed]

61. Rose, M.J.; Gray, H.B.; Winkler, J.R. Hydrogen Generation Catalyzed by Fluorinated Diglyoxime−Iron Complexes at Low Overpotentials. *J. Am. Chem. Soc.* **2012**, *134*, 8310–8313. [CrossRef] [PubMed]

62. Hu, X.; Brunschwig, B.S.; Peters, J.C. Electrocatalytic Hydrogen Evolution at Low Overpotentials by Cobalt Macrocyclic Glyoxime and Tetraimine Complexes. *J. Am. Chem. Soc.* **2007**, *129*, 8988–8998. [CrossRef] [PubMed]

63. Jacobsen, G.M.; Yang, J.Y.; Twamley, B.; Wilson, A.D.; Bullock, R.M.; Rakowski-DuBois, M.; DuBois, D.L. Hydrogen Production Using Cobalt-based Molecular Catalysts Containing a Proton Relay in the Second Coordination Sphere. *Energy Environ. Sci.* **2008**, *1*, 167–174. [CrossRef]

64. Helm, M.L.; Stewart, M.P.; Bullock, R.M.; DuBois, M.R.; DuBois, D.L. A Synthetic Nickel Electrocatalyst with a Turnover Frequency above 100,000 s^{-1} for H_2 Production. *Science* **2011**, *333*, 863–866. [CrossRef] [PubMed]

65. Winter, A.; Zsolnai, L.; Huttner, G. Dinuclear and Trinuclear Carbonyliron Complexes Containing 1,2- and 1,3-Dithiolato Bridging Ligands. *Z. Naturforsch.* **1982**, *37b*, 1430–1436. [CrossRef]

66. *APEX2 Version 2.0-2*; Bruker AXS Inc.: Madison, WI, USA, 2005.

67. *SAINT Version 7.23A*; Bruker AXS Inc.: Madison, WI, USA, 2005.

68. Sheldrick, G.M. *SADABS Version 2004/1*; University of Göttingen: Göttingen, Germany, 2004.

69. *Program XS from SHELXTL Package, V. 6.12*; Bruker AXS Inc.: Madison, WI, USA, 2001.

70. Zhao, Y.; Truhlar, D.G. The M06 suite of density functionals for main group thermochemistry, thermochemical kinetics, noncovalent interactions, excited states, and transition elements: Two new functionals and systematic testing of four M06-class functionals and 12 other functionals. *Theor. Chem. Acc.* **2008**, *120*, 215–241.

71. Frisch, M.J.; Trucks, G.W.; Schlegel, H.B.; Scuseria, G.E.; Robb, M.A.; Cheeseman, J.R.; Scalmani, G.; Barone, V.; Mennucci, B.; Petersson, G.A.; et al. *Gaussian 09, Revision A.02*; Gaussian, Inc.: Wallingford, CT, USA, 2009.

72. Dolg, M.; Wedig, U.; Stoll, H.; Preuss, H. Energy-adjusted ab initio pseudopotentials for the second and third row transition elements. *J. Chem. Phys.* **1987**, *86*, 866–872. [CrossRef]